

Virtual MIMO Wireless Sensor Networks: Propagation Measurements and Fusion Performance

I. Dey, *Member, IEEE*, P. Salvo Rossi, *Senior Member, IEEE* M. Majid Butt, *Senior Member, IEEE* and Nicola Marchetti, *Senior Member, IEEE*

Abstract—In this paper, we investigate the practical implications of employing virtual multiple-input-multiple output (MIMO) systems for prototyping future-generation wireless sensor networks, especially in the light of recently proposed distributed detection based decision fusion rules. In order to do that, an indoor-to-outdoor measurement campaign has been conducted recently for investigating the propagation characteristics of an 8×8 virtual multiple-input-multiple-output (MIMO) system. The campaign is conducted with transmit antennas representing the sensors deployed in different indoor environments and receive antennas mounted on an outside tower representing the decision fusion center. Channel measurements are reported when a 20 MHz wide signal is transmitted at 2.53 GHz. Measurements are collected for different spatial combinations of the transmit antennas. After analyzing the collected data, performance of different decision fusion rules are compared and tested over the measured channel. The results show that the fusion rules perform differently over different sets of measured channels. The results obtained here are important for maximizing performance and enabling air-interface design of next-generation wireless sensor networks.

Index Terms—Wireless sensor networks, MIMO channel measurement, Large and small scale channel characterization, Decision fusion performance.

I. INTRODUCTION

Wireless Sensor Networks (WSN) have emerged over the last few years as the backbone of a plethora of applications ranging from delivering information in rural areas, harsh industrial environments (like down-hole oil and gas industry, mining of radio-active materials etc.) and other complex scenarios (like under-ice communication in the Arctic, monitoring activities in a volcano etc.), security surveillance, emergency monitoring to body area network for advanced health care. Research to date has been followed in three main dimensions : sensing (e.g., sensor sampling), processing (e.g., data aggregation) and communication (e.g., routing and data dissemination). A remarkable characteristics of different kinds of WSN is collection and effective transportation of large amount of information to the fusion center (FC) for performing data fusion to arrive at a decision on an observation, estimation of a situation or detection of a particular phenomenon.

A. Motivation

Use of multi-antenna technology at the FC has recently been proposed [1], [2] to cope with intrinsic interference and

I. Dey and N. Marchetti are with CONNECT, Trinity College Dublin, Ireland (E-mail: deyi@tcd.ie; marchetn@tcd.ie).

P. Salvo Rossi is with Norwegian University of Science and Technology, Trondheim, Norway (E-mail: salvorossi@ieee.org).

M. Majid Butt is with Nokia Bell Labs, France (E-mail: majid.butt@ieee.org).

deep fading over the multiple access channel (MAC) used for communication between the sensors and the FC. Thus multiple sensors communicating with the multi-antenna FC over a MAC result in a ‘virtual’ multiple-input-multiple-output (MIMO) channel between the sensors and the FC. Several decision fusion (DF) rules have been proposed in [3], [4] and compared and evaluated based on the assumption that fading statistics follow Gaussian or Rayleigh distribution. Only the works in [2], [5] takes into account pathloss and shadowing in the considered channel model.

The performance of channel-aware fusion rules and the overall sensor network is heavily dependent on the propagation statistics of the channel between the sensors and the FC. For example, the fusion rule statistics in many cases are proportional to channel coefficients (comprising of both large and small scale statistics) and are dependent on the instantaneous channel state information (CSI) [6], [7]. In terms of the entire network performance, properties like latency, energy efficiency etc., are all adversely affected by using inadequate fading distributions in the system design [8]. Furthermore, the network may encounter diverse channel conditions between each local center and the FC depending on the spatial distribution of the sensors, the environment in which the sensors are deployed, and the environment around the receive antennas.

Despite the significance of the propagation statistics, only a few channel measurement campaigns have been performed for WSNs over the years. The few that are conducted are generally environment or application specific. Small scale fading characteristics in inter-sensor channels are studied in depth for indoor [9], industrial [10], multi-chamber metal environments [11] or oil reservoirs [12]. In each case, the communication devices are all located in the same environment, especially indoor. To the best of our knowledge, there is no in-depth experimental investigation of the channel statistics (both small scale and large scale statistics) of the propagation channel between multiple sensors and FC equipped with single or multiple antennas. Neither similar studies have been conducted when the transmit sensors and receive sink nodes are located in different environments i.e. indoor and outdoor respectively or vice-versa.

B. Related Works

Distributed detection using DF has been extensively investigated for WSNs [13]–[15]. Suboptimal rules have been applied to both parallel access channel (PAC) [16] and MAC [17] scenarios. In case of a PAC architecture, the sensors are assigned orthogonal parallel channels for transmission. In case of MAC,

the advantage of using multiple antennas is exploited in [1]. Several DF rules like, Maximal Ratio Combining (MRC), Chair-Varshney Maximum Likelihood (CV-ML), Equal Gain Combining (EGC), MaxLog and Chair-Varshney Minimum Mean Squared Error (CV-MMSE) rules have been analyzed both for the PAC [18], [19] and MAC [20], [21] scenarios.

For both PAC and MAC, MRC and CV-ML, fusion rules approach optimum performance only at very low and very high link signal-to-noise ratios (SNRs) respectively, with EGC as the robust choice over the entire SNR range [22] and MaxLog as the champion over all the mentioned rules [23]. Though employing multiple antennas at decision fusion center (DFC) is profitable for all rules, all of them exhibit a saturation point for the probability of correct detection depending on the channel SNR [1].

Due to the wonderland of performance improvement promised by MIMO systems, a lot of measurement campaigns have been conducted to characterize the propagation channel. In recent years, the major focus has been angular spreads [24], [25] indoor-to-indoor [26], outdoor-to-outdoor [27] and outdoor-to-indoor [28] environments. This emphasis is due to the fact that the number of antenna elements in each link is limited and the dispersion in elevation is much smaller than the dispersion in azimuth.

The most detailed and generalized measurement-based MIMO channel model to date is the WINNER II channel model [29]. It is based on geometry-based stochastic channel modelling approach, independent of the antenna configurations and element patterns. It covers a plethora of communication environment including outdoor-to-indoor, indoor-to-outdoor and indoor-only scenario. The model is scalable from SISO or MIMO links to a multi-link MIMO scenario. However, the WINNER II model is not scalable to virtual MIMO scenario which exploits array processing in order to improve performance through diversity gain from multiple antennas.

Virtual MIMO systems have been introduced [30] to improve data-rate in a wide-area MIMO system by allowing multiple users to cooperate. Propagation modeling efforts in virtual MIMO includes inter-base-station cooperation measurements of capacity in [31], comparison of MIMO and single-input-single-output (SISO) links in [32], outdoor-to-indoor cellular scenario in [33] and antenna selection for multi-user (MU)-MIMO based distributed antenna systems in [34]. However, propagation modeling in [34] is executed for WLAN application based on ray-tracing and therefore, is application-specific and location-specific.

C. Contribution

In this paper, we present results on a first-of-a-kind indoor-to-outdoor measurement campaign intended for capturing propagation characteristics in a virtual MIMO WSN and comparing performances of different DF rules over the measured virtual MIMO channels. In this study, we focus on pathloss, large scale shadowing and small scale fading characteristics for each measurement location and scenario. The results obtained here can be directly incorporated in realistic next-generation

WSN air-interface design. The main contributions of this paper are summarized as below :

- We conduct a detailed measurement campaign to characterize the propagation channel between multiple sensors and DFC equipped with multiple antennas. We present results for a fully loaded case, where the number of sensors is equal to the number of receive antennas. But from the recorded data, we can easily characterize the propagation channel for the cases where the number of sensors is less than the number of receive antennas (underloaded) and where the number of sensors is more than the number of receive antennas (overloaded). The results obtained can also be extended to the case where the DFC is equipped with a single antenna.
- We present here a first-of-a-kind measurement campaign where the transmitter nodes are deployed in an indoor environment and the receive antennas are located outdoor. Half-omnidirectional single antennas are used to represent transmit sensor nodes and receive antennas are co-located on a tower representing the DFC. Both static and dynamic conditions have been taken into account and two different indoor scenarios are considered, one office-like room and one instrumentation room. Due to channel reciprocity, the same channel statistics can be employed to characterize the propagation channel between outdoor sensors and indoor DFC.
- Both large and small scale statistics are derived from the data collected over each measurement route, location and spatial distribution of the transmit nodes. The large scale shadowing variability is found to be unchanged for all measurement sets and shown to follow lognormal distribution. The fading statistics are found to be well described by either Ricean distribution, two-wave with diffused power (TWDP) distribution or double Rayleigh distribution depending on the measurement scenario and environment.
- The large and small scale channel characteristics extracted from the campaign are incorporated in the performance analysis of two sets of fusion rules, Decode-and-fuse and Decode-then-fuse. The first group includes MRC, EGC and MaxLog rules. The second group includes CV-ML and CV-MMSE. In this context, our work is the first attempt to compare and test the applicability of the fusion rules in realistic environment. Performance of other fusion rules (optimum and sub-optimum) that do not fall in the above-mentioned groups can also be analyzed, compared and tested using the procedure presented in this paper.
- The results demonstrate different performance behaviors of the decision fusion rules on the measured data. We show that MRC and EGC perform close to each other in realistic scenario. CV-MMSE outperforms all other rules confirming the observations in [1]. MaxLog performs worse than the other two Decode-and-fuse rules considered here.

The paper is organized as follows: Section II details the measurement set-up, scenario and the process by which in-

formation is extracted from the collected data. Section III provides results from analyzing the collected measurements. Section IV compares performances of different DF rules in realistic environment using the channel statistics derived from the measurement, while Section V concludes the paper.

Notations: Lower-case (resp. upper-case) bold letters denote vectors (resp. matrices), with a_k (resp. $a_{n,m}$) representing the k th element (resp. (n,m) th element) of \mathbf{a} (resp. \mathbf{A}); $(\cdot)^t$ denotes transpose, $E\{\cdot\}$, $\angle(\cdot)$, $(\cdot)^\dagger$, and $\|\cdot\|$ represents expectation, phase, conjugate transpose and Frobenius norm operators, respectively; \ln represents the natural logarithmic function; \mathbf{I}_N denotes the $N \times N$ identity matrix; $\mathbf{0}_N$ (resp. $\mathbf{1}_N$) denotes the null (resp. ones) vector of length N .

II. MEASUREMENT CAMPAIGN

This section is dedicated for providing detailed description of the set of equipments used for collecting measurement (Subsection II-A); the environment, set-up and the scenarios in which the measurements are accumulated (Subsection II-B) and; the process of analyzing the measurements and extracting the statistical information on the propagation environment from them (Subsection II-C).

A. Measurement Equipment

This subsection articulates the details of the ensemble of equipments used to conduct a measurement campaign at Facility of Over-the-Air Research and Testing (FORTE) facility of Fraunhofer IIS in Ilmenau, Germany. In this campaign, the time-varying channel impulse responses (CIRs) of 8×8 distributed multiple-input-multiple-output (MIMO) channels are measured at 2.53 GHz with 20 MHz bandwidth and sub-carrier spacing of around 0.15 MHz. Measurement was done in the 2.5 GHz band owing to its popularity as the operating frequency in WSNs and implementation flexibility due to the abundance of commercially available sensor and actuator devices in that band. The 8×8 case models the fully-loaded (number of sensors, S = number of receive antennas at the decision fusion center (DFC), N) communication scenarios in wireless sensor networks (WSNs).

For each measurement set, the 8 half-omnidirectional (directional with half power beamwidth of 180 degrees) transmit antennas emulating sensors are deployed simultaneously. They are fixed at different heights, namely a) near the ceiling, b) near the ground and c) at the heights of 1m, 1.5m and 2m. They are distributed at different locations namely, a) on all 4 walls, b) on only 3 walls, c) only on 1 wall at a time etc. The antennas are positioned in two rooms of the FORTE building.

The antennas on the receive side are mounted at a height of around 48m on a tower. Four different dual-polarized antennas are used for reception where both the polarization in each case are activated to have functionally effective 8 antennas on the receive side. The receive antennas set-up on the tower are arranged in two columns, two antennas on each row and they receive signals with $\pm 45^\circ$ polarizations.

An overview of the measurement set-up is provided through the block diagram in Fig. 1. The transmit and receive antennas are connected to a MEDAV RUSK-HyEff MIMO Channel Sounder via optical fibers, control cables, and transmit and

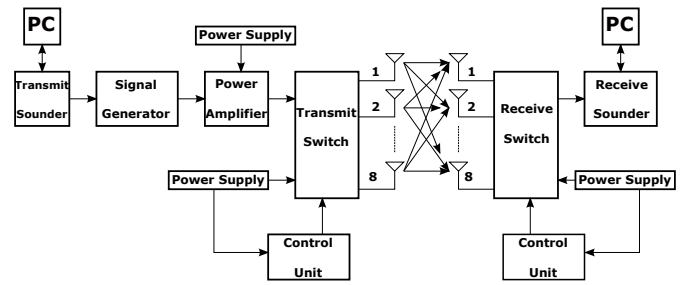


Fig. 1. Block diagram of measurement set-up.

receive switches. The channel measurements are conducted and recorded using this channel sounder. On the transmit side, the length of the test signal is adjusted according to the observation time of the wireless propagation channel between the transmitter and the receiver. Using arbitrary waveform generated by a Rhode & Swartz RSSMU200 signal generator, the test signal is distributed to the transmit antennas via up-converter, power amplifier and multiplexer. The test signal is transmitted from each of the 8 transmit antennas with different time offsets to ensure orthogonality. Let the 8 sequences be denoted by $p_1[m], p_2[m], \dots, p_8[m]$, where m is the length of the multi-tone signal.

A maximum transmit power of 44 dBm is fired at the output of the power amplifier. For sufficient signal-to-noise ratio (SNR) calibration, the transmit and receive sounders are connected directly to each other with a cable that includes 100 dB of attenuation. The measured SNR is obtained as 40.7 dB which can be shown to be sufficient enough to yield nominal measurement error following the methods in [35]. This will ensure that the measurement error will have no effect on the study of channel measurements.

The received radio frequency (RF) signal is down-converted to Intermediate Frequency (IF) to 90 MHz and subsequently processed and stored for offline analysis. The receiver continuously performs correlations of the received signal with copies of $p_1[m], p_2[m], \dots, p_8[m]$. As a result, a new 8×8 MIMO channel response is captured every $6.4 \mu\text{s}$. Phase synchronization is achieved through Rubidium frequency reference. Clock-signal synchronization is accomplished by connecting the two 10 MHz clocks of transmit and receive sounders using an optical fiber. It is worth-mentioning here that a 200 ns delay is still incurred due to the reception cable from the switch and antennas to the sounder.

B. Measurement Environment

Two different rooms in the FORTE building are selected, of which, one is located on the 2^{nd} floor (Conference Room, \mathcal{C}) and the other is located on the 1^{st} floor (Instrumentation Room, \mathcal{I}) of the building. The room \mathcal{C} is 8.45m long, 4.52m wide and 2.75m high, while the room \mathcal{I} is 5.7m long, 3.5m wide and 3m high. These rooms are chosen such that a wide variety of indoor communication environments can be measured and characterized. Some of the interesting scenarios include room with keyhole effect (no windows) and with no direct line-of-sight (LOS) communications, conference room (with both direct LOS and non-LOS (NLOS) communication

path) and room cluttered with several noisy electrical metering equipment, etc. (potential scenarios for future industrial automation).

From the room upstairs (\mathcal{C}) each measurement set is repeated for a) a stationary scenario and b) a dynamic scenario with people moving on a defined track through the scenario. For the static scenario, each measurement set is recorded for 1000 snapshots, each snapshot being $6.4 \mu\text{s}$ long. In case of dynamic scenario, measurement is recorded for the time duration as long as it takes for one person to walk through the entire room (around 19-20 secs). For the room downstairs (\mathcal{I} with no windows), each measurement set is conducted only for the stationary scenario due to the improbability of any dynamic scenario in a factory/instrumentation environment. In this case, each measurement set is recorded for 5000 snapshots.

The first set of measurements are collected in the rooms (\mathcal{C} & \mathcal{I}) for the cases where all the transmit antennas are deployed at the same height on all 4 walls at one time (refer to Fig. 2(a) for $\mathcal{C}1, \mathcal{C}2, \mathcal{C}3, \mathcal{C}4$ and Fig. 2(e) for $\mathcal{I}1, \mathcal{I}2, \mathcal{I}3, \mathcal{I}4$) with $\mathcal{C}1$ & $\mathcal{I}1$: all antennas near the ground, $\mathcal{C}2$ & $\mathcal{I}2$: all antennas at a height of 1m from the ground, $\mathcal{C}3$ & $\mathcal{I}3$: all antennas at a height of 2m from ground and $\mathcal{C}4$ & $\mathcal{I}4$: all antennas near the ceiling. The second set of measurements are also recorded in both the rooms where all the transmit antennas are positioned at different heights on one wall at one time (refer to Fig. 2(b) for $\mathcal{C}5, \mathcal{C}6, \mathcal{C}7, \mathcal{C}8$ and Fig. 2(f) for $\mathcal{I}5, \mathcal{I}6, \mathcal{I}7, \mathcal{I}8$) with $\mathcal{C}5$ & $\mathcal{I}5$: all antennas on Wall 1, $\mathcal{C}6$ & $\mathcal{I}6$: all antennas on Wall 2, $\mathcal{C}7$ & $\mathcal{I}7$: all antennas on Wall 3 and $\mathcal{C}8$ & $\mathcal{I}8$: all antennas on Wall 4.

The third set of measurements refer to the scenarios where all the antennas are distributed at different heights on all 4 walls following 4 sets of combinations (refer to Fig. 2(c) for $\mathcal{C}9, \mathcal{C}10, \mathcal{C}11, \mathcal{C}12$ and Fig. 2(g) for $\mathcal{I}9, \mathcal{I}10, \mathcal{I}11, \mathcal{I}12$). The last set of measurements are accumulated in the rooms with antennas at different heights only on 3 walls (refer to Fig. 2(d) for $\mathcal{C}13, \mathcal{C}14, \mathcal{C}15$ and Fig. 2(h) for $\mathcal{I}13, \mathcal{I}14, \mathcal{I}15$). Only Wall 3 is avoided in both the rooms as it is completely out-of-sight of the communication path in both cases between the transmit and receive antennas.

C. Data Analysis

The impulse response of the channel between transmit antenna s and the receive set of antennas is represented by the matrix $\mathbf{h}_s \in \mathbb{C}^{N \times L}$ where N is the number of receive antennas and L is the number of discrete channel taps ($L = 1000$ for each static and $L = 5000$ for each dynamic scenario). The element in row n and column l of \mathbf{h}_s is denoted by $h_s(n, l)$.

If the average received power from transmit antenna s at location i is calculated as $P_{R,s}(i) = \frac{1}{N} \sum_n \sum_l |h_s(n, l)|^2$, then average attenuation is given by,

$$A_s(i) = P_{R,s}(i) / (\alpha P_T) \quad (1)$$

where P_T is the system transmit power and α includes cable and other system losses determined during system calibration.

Path-loss exponent (ν) is determined from the best fit line of a log-log plot of distance versus $A_s(i)$. The shadowing distribution can be obtained by plotting the pdf of the values of deviation of each $A_s(i)$ value from the best fit line in

the log-log plot. For each measurement location, there are 8 attenuation values, $\mathbf{A}(i) = [A_1(i), A_2(i), \dots, A_8(i)]$, since 8 separate antennas acting as $S = 8$ different sensors are used.

To characterize the small scale fading statistics, first of all the power delay profile (pdp) of the channel is extracted. It is done by averaging the power s along the n -axis to yield an L -element vector for each transmit antenna. The mean excess delay is the first moment of each pdp given by,

$$\bar{\tau}_s = \frac{\sum_l \tau_s(l) \left(\frac{1}{N} \sum_n |h_s(n, l)|^2 \right)}{\sum_l \left(\frac{1}{N} \sum_n |h_s(n, l)|^2 \right)} \quad (2)$$

The root-mean-squared (rms) delay spread is the square root of the second central moment of each pdp calculated as,

$$r_s = \sqrt{\bar{\tau}_s^2 - (\bar{\tau}_s)^2} \quad (3)$$

where $\bar{\tau}_s^2 = \frac{\sum_l \tau_s^2(l) \left(\frac{1}{N} \sum_n |h_s(n, l)|^2 \right)}{\sum_l \left(\frac{1}{N} \sum_n |h_s(n, l)|^2 \right)}$. The corresponding channel coherence bandwidth for each transmit antenna is calculated according to $1/(5r_s)$ [38].

The small scale fading statistics can be determined by using the frequency domain response extracted from the sounder. Let $H_s(n, f)$ denote the output frequency response where f is the discrete frequency index. The channel frequency response matrix is denoted by $\mathbf{H}_s \in \mathbb{C}^{N \times L}$ where $H_s(n, f)$ is the element on the n th row and f th column of \mathbf{H}_s .

If $B_{\text{coh},s}$ denotes the discrete coherence bandwidth of the channel between the s th transmit antenna and the receiver and B_{sig} is the discrete bandwidth of the measurement signal, the number of frequency response values experiencing independent small scale fading can be calculated as, $R_s = \lfloor B_{\text{sig}} / B_{\text{coh},s} \rfloor$. As N fading values are obtained at each of the frequency points, the $1 \times NR_s$ fading vector for the s th transmit antenna can be computed as,

$$\text{vec}(\Xi_s) = [|H_s(0, 0)|, \dots, |H_s(N-1, 0)|, |H_s(0, B_{\text{coh},s})|, \dots, |H_s(N-1, R_s B_{\text{coh},s})|] \quad (4)$$

Chi-squared goodness-of-fit test is applied to each of the fading vectors, $\text{vec}(\Xi_s)$, for each sensor for small scale fading analysis against three different fading distributions, namely, the Rician, double-Rayleigh and two-wave with diffused power (TWDP) distributions. A significance level of 10% [36] is applied to each measurement set for verification of goodness of fit. First of all, double-Rayleigh distribution is applied to every measurement set. The data sets that do not fit double-Rayleigh are checked against Rician and TWDP distributions. For both cases K -factor is compiled using the method of moments [37]. Only those measurements that agree with Rician and TWDP distributions are included in the K -factor plots presented in Subsection III-B.

Antenna correlation is calculated by determining the correlation coefficients between each pair of fading vectors to yield an 8×8 correlation coefficient matrix for each measurement set-up,

$$\Upsilon_\xi = \begin{bmatrix} \xi_{1,1} & \xi_{1,2} & \cdots & \xi_{1,8} \\ \xi_{2,1} & \xi_{2,2} & \cdots & \xi_{2,8} \\ \vdots & \vdots & \ddots & \vdots \\ \xi_{8,1} & \xi_{8,2} & \cdots & \xi_{8,8} \end{bmatrix} \quad (5)$$

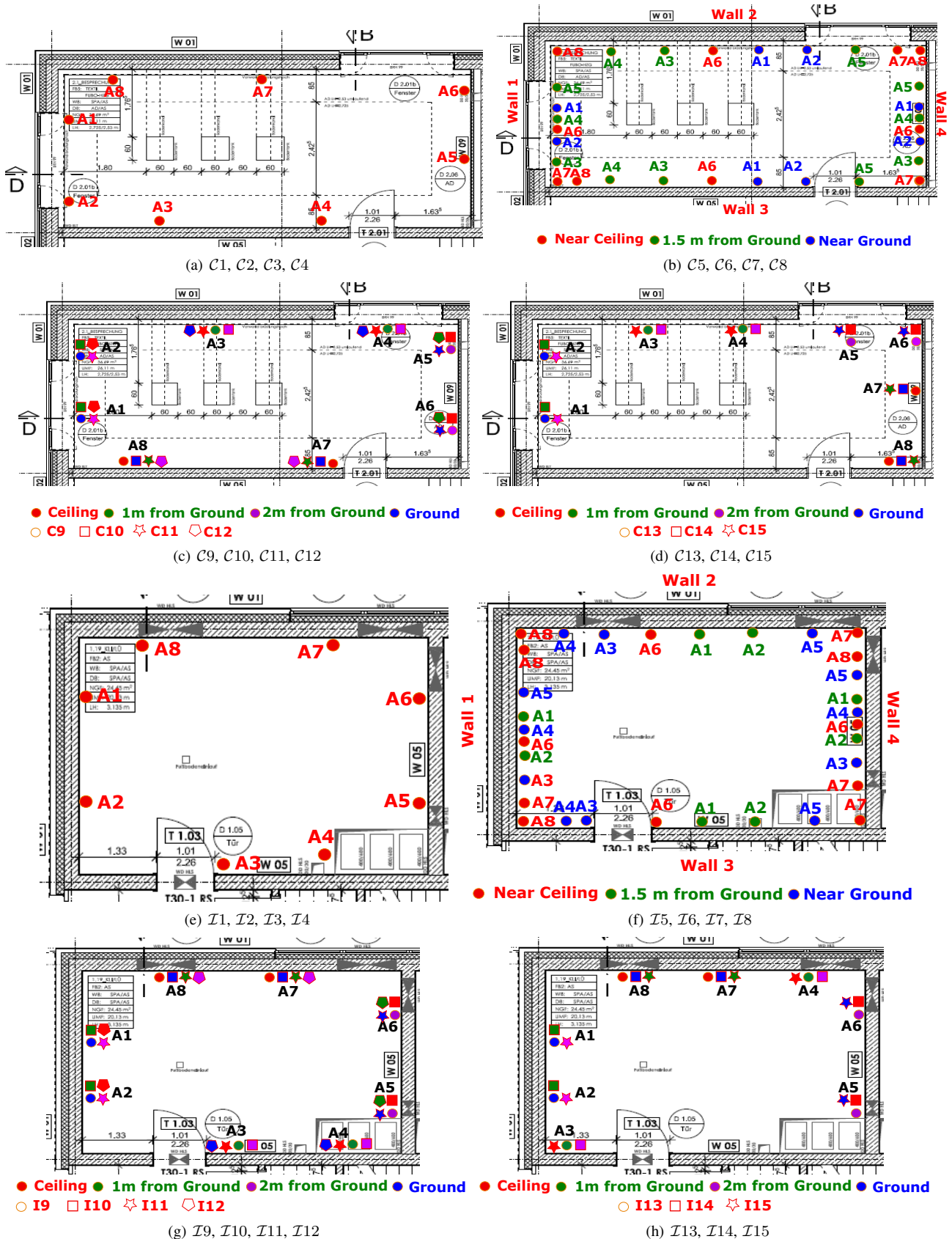


Fig. 2. Measurement Set-ups : Conference Room and Instrumentation Room with 8 transmit antennas denoted by A_1, A_2, \dots, A_8 .

where $\xi_{e,f}$ is the correlation coefficient between $\text{vec}(\Xi_e)$ and $\text{vec}(\Xi_f)$ and $\xi_{e,e}$ is the auto-correlation coefficient of $\text{vec}(\Xi_e)$.

Amount of Fading (AF) is a unified measure for the severity of fading that directly utilizes the moments of the fading distribution itself and is given by, $AF = \frac{\text{Var}(\alpha^2)}{(\text{E}\{\alpha^2\})^2}$, where α is the instantaneous fading amplitude of a complex fading channel. To quantify AF for each measurement set, here we use $\mathcal{A}_s = \text{Var}((\text{vec}(\Xi_s))^2) / \{\text{E}\{(\text{vec}(\Xi_s))^2\}\}^2$. AF is an efficient measure of the intensity of fading experienced as it can be calculated directly from the fading vectors of the transmit antennas. It is to be noted here that we have calculated only the temporal AF for each measurement set.

We also use the phase information obtained from the complex CIR to calculate steering vector for each transmit antenna. We will use the steering vectors in Section IV to formulate fading vectors for the propagation channel. If the s th transmit antenna is seen as a point-like source by the receive set of antennas, then the steering vector from the s th antenna $\mathbf{U}(\phi_s)$ can be computed from,

$$\mathbf{u}(\phi_s) = [1 e^{j\pi \cos(\phi_s)} e^{j\pi 2 \cos(\phi_s)} \dots e^{j\pi(N-1) \cos(\phi_s)}] \quad (6)$$

where $\phi_s = \frac{1}{N} \sum_n \sum_l \angle h_s(n, l)$. Therefore for each measurement set, there will be 8 such steering vectors given by, $\mathbf{U}(\Phi) = [\mathbf{u}(\phi_1), \mathbf{u}(\phi_2), \dots, \mathbf{u}(\phi_8)]$, since each transmit antenna generates a separate steering vector.

D. Note on Wifi Interference

Due to widespread Wifi access points located in the building using the frequency bands closer to our measurement bands of 2.45 GHz and 2.5 GHz, some distortions appeared in the recorded CIRs due to random fluctuations of the inherent Automatic Gain Control (AGC) and the channel estimates within the measurement equipment. The AGC tries to cope with the interference power but is limited to 3dB increase/decrease per snapshot. When the AGC reaches its highest value, distortion is gone. So the execution of the distorted data is mandatory to gain clear and realistic channel characterization. In this campaign, the exclusion of the distorted data is done based on the shape of the CIR. Each snapshot is carefully investigated using sampled channel frequency response and AGC value plots. Comparing both the plots, the distortion is removed to extract clean data.

III. MEASURED MIMO CHANNELS

Here we present the results from our analyses of the collected measurements. Subsection III-A presents the details on the derived large scale statistics while Subsection III-B provides the small scale characterization.

A. Large-Scale Statistics

The log-log attenuation plots and the corresponding shadowing distributions for three different measurement scenarios, static environment - Conference (SC), dynamic environment - Conference (DC) and static environment - Instrumentation (SI) rooms are presented in Fig. 3, Fig. 4 and Fig. 5 respectively. Table I provides the pathloss exponents (η_P) and mean and standard deviation (μ_P , σ_P) of the shadowing distributions. The pathloss and shadowing values are calculated

TABLE I
LARGE SCALE PARAMETERS

Scenario	η_P	μ_P (dB)	σ_P (dB)
SC	2.72	1.22	2.4
SI	3.96	1.48	1.89
DC	2.56	1.77	3.6

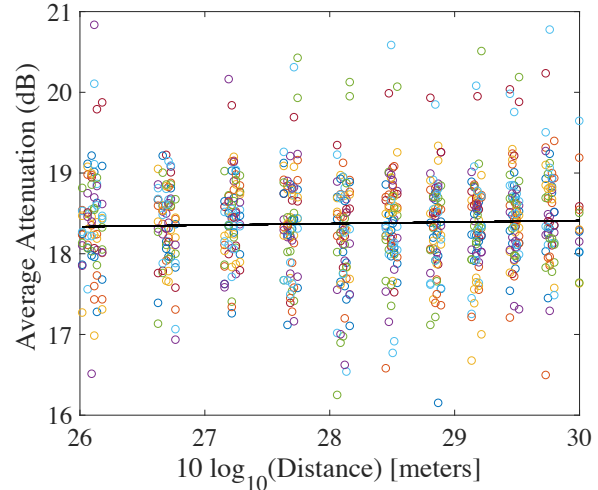


Fig. 3. Log average attenuation versus log distance for Conference - Static environment.

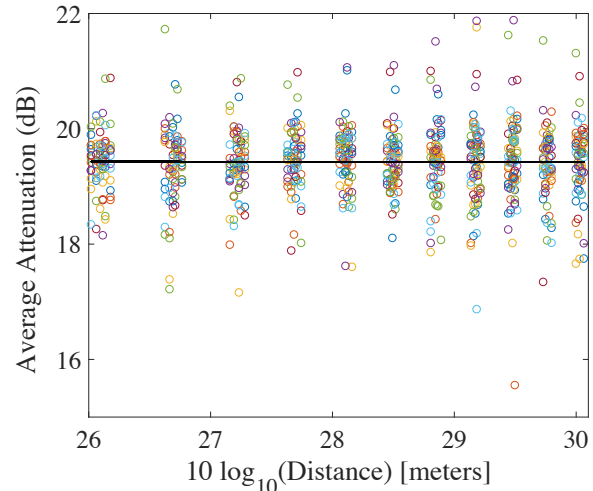


Fig. 4. Log average attenuation versus log distance for Conference - Dynamic environment.

for each measurement set. Average values of η_P , μ_P and σ_P are grouped by the type of the measurement location and scenario. The shadowing distributions for all the environments are presented in Fig. 6.

A very small variation in shadowing is observed between different environments. Higher shadowing is experienced in the C room than the I room. The reason can be attributed to the fact that in spite of the windowless I room being cluttered with several equipments, most of these equipments are metallic. Hence, a considerable amount of signal power is received even over obstructed propagation links. The opposite trend is observed for the pathloss exponents. Higher η_P is experienced over the link between I room and the receive set

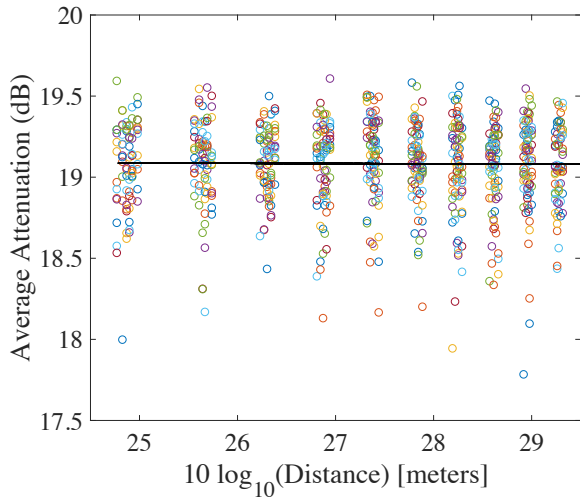


Fig. 5. Log average attenuation versus log distance for Instrumentation - Static environment.

of antennas on the tower. The \mathcal{C} room is on the second floor of the building and therefore, the actual distance between the \mathcal{C} room and the receive antenna set is less than between \mathcal{I} room and the receiver.

All the measurement environments experience shadowing with approximately lognormal distribution. The incomplete Gamma function is used for verification of goodness of fit between lognormal and extracted shadowing distributions, where \mathcal{Q} is the probability that a value of chi-square as poor as the shadowing value occur by chance given by,

$$\mathcal{Q}\left(\frac{N-2}{2}, \frac{\chi_1^2}{2}\right) = \frac{1}{\Gamma\left(\frac{N-2}{2}\right)} \int_{\frac{\chi_1^2}{2}}^{\infty} e^{-\nu_P} \nu_P^{\left(\frac{N-2}{2}\right)-1} d\nu_P \quad (7)$$

with N as the number of shadowing values experienced, ν_P is the lognormally distributed shadowing variable and χ_1^2 is the Chi-squared merit function [36]. If the \mathcal{Q} -value is larger than 0.1, the distribution fitting is fine under any condition. When it is smaller than 0.1 but larger than 0.001, the distribution fitting is fine if the measurement errors are non-normal or have been moderately underestimated. If \mathcal{Q} -value is less than 0.001, the model and/or the estimation procedure is questionable. In this case, all the recorded \mathcal{Q} -values fall between 0.25 and 0.85 which confirm the accuracy of the distribution fitting.

B. Small-Scale Fading Statistics

First of all, Chi-square goodness-of-fit is used to determine the suitable distribution that can accurately characterize the small scale fading statistics in each measurement set. There are in total 42 sets of measurements recorded, with 15 for \mathcal{SC} , 15 for \mathcal{DC} and 12 for \mathcal{SI} scenarios. Out of the 15 sets recorded over \mathcal{SC} , small scale statistics fit Ricean distribution in all cases. Out of the 15 sets recorded over \mathcal{DC} , small scale statistics fit two-wave with diffused power (TWDP) distribution in 12 cases, and out of the 12 sets recorded over \mathcal{SI} , small scale statistics fit double Rayleigh distribution in 9 cases. The proportion of the measurements that fits the double-Rayleigh distribution is $(9/42) = 21.4\%$. Proportions of measurements

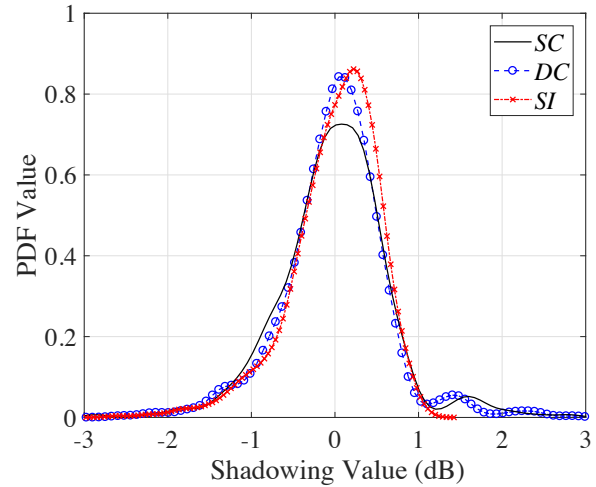


Fig. 6. Shadowing Distributions for all environments.

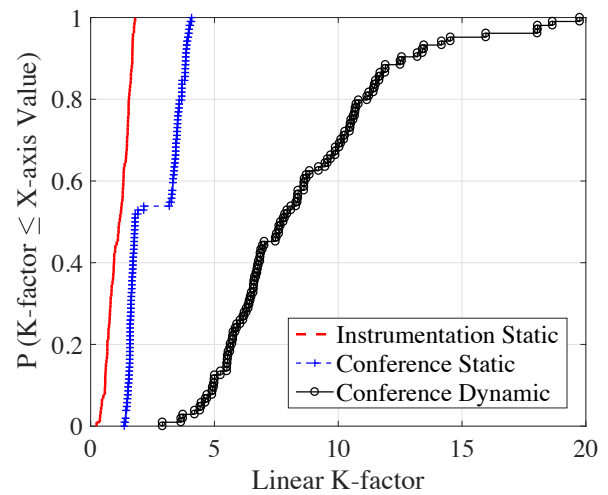


Fig. 7. CDF of K -factor for all environments.

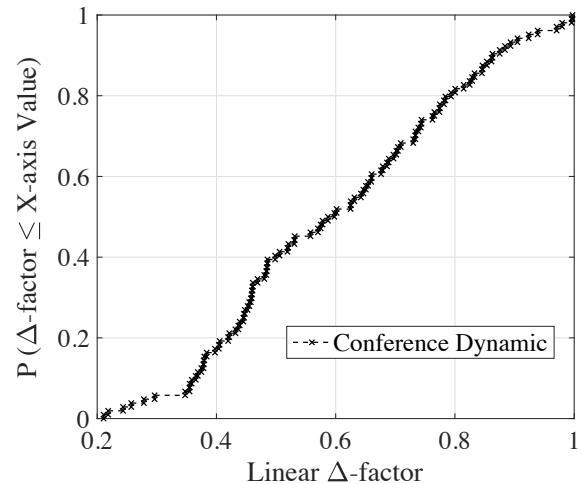


Fig. 8. CDF of Δ for the dynamic environment in the conference room.

following TWDP distribution is $(12/42) = 28.6\%$ of all recordings. The rest $(21/42) = 50\%$ of the measurements fits the Ricean distribution.

The K -factors for the measurements that fit the Ricean and TWDP distributions are included in Fig. 7 and Δ values from

TABLE II
SMALL SCALE PARAMETERS

Scenario	K	Δ	$\xi_{e,f}$	\mathcal{A}
\mathcal{SC}	2.5424	0	0.6511	7.64
\mathcal{SI}	1.1217	0	0.5877	3.8158
\mathcal{DC}	8.5287	0.6004	0.41	4.5227

TABLE III

GENERALIZED RANGE OF VALUES SMALL SCALE PARAMETERS

Scenario	K	Δ
\mathcal{SC}	0.5 to 4	-
\mathcal{SI}	0	-
\mathcal{DC}	6 to 20	0.1 to 0.9

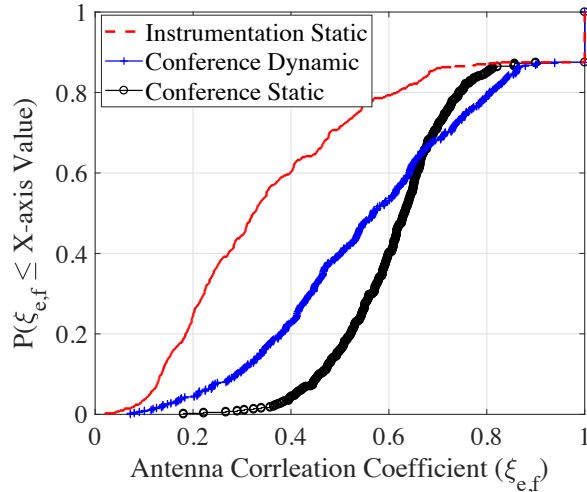


Fig. 9. CDF of Antenna Correlation Coefficient for all environments.

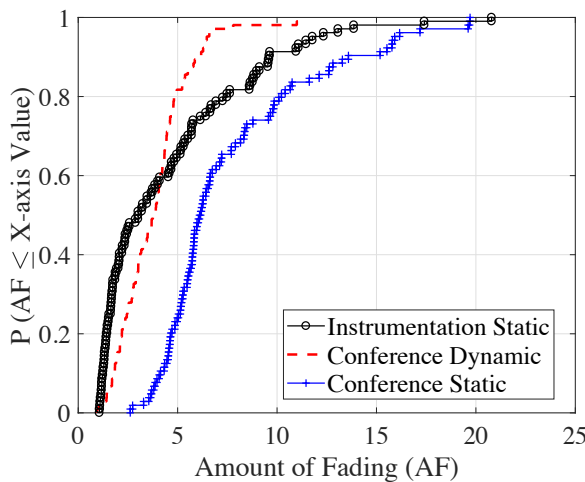


Fig. 10. CDF of Amount of Fading (AF) for all environments.

the fitted TWDP distributions are included in Fig. 8. Linear Δ -factor was introduced as a parameter of TWDP distribution. TWDP characterizes fading due to the interference of two strong radio signals and numerous smaller diffuse signals. Physically, Δ ($= 0$ to 1) is the shape factor of the TWDP distribution quantifying the disparity between the two strong radio signal components and can be calculated as $\Delta = \frac{2V_1V_2}{V_1^2+V_2^2}$, where V_1 and V_2 are the instantaneous amplitudes of the specular components. Table II provides the average values of K , Δ , $\xi_{e,f}$ and AF (\mathcal{A}) for the measurement scenarios of \mathcal{SC} , \mathcal{DC} and \mathcal{SI} . Antenna correlation coefficient and AF values for all the recorded measurement scenarios are plotted in Fig. 9 and Fig. 10 respectively.

Double-Rayleigh fading ($K = 0$) is experienced in the \mathcal{I} room. The \mathcal{I} room does not have any windows. The only un-

obstructed propagation link between the transmit antennas in the \mathcal{I} room and the receive antennas is through the single door of the room and subsequently through the glass doors of the building. This creates a waveguide like propagation channel. It results in a rich scattering environments without the existence of any direct LOS propagation link, traditionally referred to as 'keyhole' and 'pinhole' effect. Diffraction around edges of several metallic chambers and equipments also contribute to the keyhole effect. Hence, the measurement set encountered in such a scenario fits double Rayleigh.

The TWDP fading ($K = 6$ to 20 and $\Delta = 0.1$ to 0.9) is experienced in the \mathcal{C} room when measurement is collected in a dynamic scenario. Several direct LOS paths occur over the communication links between the \mathcal{C} room and the receive antennas through several glass windows and doors. In addition, moving human body in the dynamic scenario results in a second set of multipath components. The TWDP distribution fading model comprises of two specular multipath components in the presence of diffusely propagating waves [39]. In the \mathcal{DC} scenario, in most cases, two sets of specular multipath components arrive at the receiver, one owing the LOS communication and the other owing to the reflection from the moving body. Hence, such measurement scenario can be characterized by the TWDP distribution, a worse than Rayleigh fading case.

The rest of the measurement sets are well approximated with Ricean distribution ($K = 0.5$ to 4). This is due to the fact that for any pair of antennas, there exists a LOS path. However, multiple LOS paths can be exhibited by multiple transmit antennas owing to their different spatial locations. As a result, a bunch of direct LOS paths arrive at the receive antennas from the transmit antennas of the \mathcal{C} and \mathcal{I} rooms. It is also noteworthy here that both rooms suffer from similar AFs due to the large separation between the transmit and receive antennas, and close proximity of most of the scattering objects to the transmit antennas.

From CDF plots of antenna correlation coefficients in Fig. 9, it is evident that the lowest correlation is encountered in the static environment of room \mathcal{I} . This is in agreement with the observation made from the small scale fading (double-Rayleigh distribution) characteristics encountered in this particular scenario. Rich scattering and diffraction around the transmit antennas lead to low correlation between signals from the distributed nodes resulting in keyhole effect.

After extensive data fitting, it is possible to recommend small-scale fading parameters that are suitable for different indoor-to-outdoor communication scenarios in virtual MIMO based WSNs. The different ranges of values for K parameter of Ricean distributed channels; and K and Δ parameters of TWDP distributed channels between sensors and DFC have been compiled in Table III.

IV. FUSION PERFORMANCE ANALYSIS

This section provides a comparison of performances of different decision fusion rules over a set of measured distributed MIMO channels in a WSN with sensors that offer identical local decisions.

A. System Model and Performance Measures

Let us consider a WSN with S sensors communicating with a DFC equipped with N receive antennas. In such a network, a binary local decision taken by the s th sensor, d_s , on an observed phenomenon is mapped to a symbol $x_s \in X = \{0, 1\}$ representing an On-and-Off Shift Keying (OOK) modulation. Irrespective of the scenario and target, we assume that $d_s = \mathcal{H}_i$ maps into $x_s = i, i \in \{0, 1\}$, where $\mathcal{H}_i \triangleq \{\mathcal{H}_0, \mathcal{H}_1\}$ is the set of binary hypotheses with $\mathcal{H}_0/\mathcal{H}_1$ representing the absence or presence of a specific target. The communication links are assumed to be a flat-fading multi-access distributed (or virtual) MIMO channel with perfect synchronization at the receive end. Let us also denote the composite channel coefficient between the s th sensor and the n th receive antenna at the DFC by $\sqrt{b_{s,s}}h_{n,s}$. After matched filtering and sampling at the DFC, the received signal can be represented as,

$$\mathbf{y} = \mathbf{H}\sqrt{\mathbf{B}}\mathbf{x} + \mathbf{w} \quad (8)$$

where $\mathbf{y} \in \mathbb{C}^N$, $\mathbf{x} \in X^S$ and $\mathbf{w} \sim \mathcal{N}_C(\mathbf{0}_N, \sigma_w^2 \mathbf{I}_N)$ are the received signal, transmitted signal and the AWGN vectors respectively and $\mathcal{N}_C(\lambda, \Sigma)$ denote circular symmetric complex normal distribution with mean vector λ and covariance matrix Σ respectively. The matrices $\mathbf{H} \in \mathbb{C}^{N \times S}$ and $\mathbf{B} \in \mathbb{C}^{S \times S}$ represent the independent small scale fading and large scale attenuation with shadowing respectively. The s th diagonal element of the attenuation matrix $\mathbf{B} \triangleq \text{diag}([\beta_1, \beta_2, \dots, \beta_S]^T)$ accounts for pathloss and shadowing experienced by the s th sensor.

The fading vector of the s th sensor can be given by,

$$\mathbf{h}_s^{\text{Rice}} = \kappa_s \mathbf{u}(\phi_s) + \sqrt{1 - \kappa_s^2} \check{\mathbf{h}}_s \quad (9)$$

which forms the s th column of \mathbf{H} and $\mathbf{u}(\cdot)$ denotes the steering vector with $\check{\mathbf{h}}_s \sim \mathcal{N}_C(\mathbf{0}_N, \mathbf{I}_N)$ typifying the NLOS (scattered) component and $\kappa_s \triangleq \sqrt{\frac{K_s}{1+K_s}}$. Here K_s is the Rician K -factor between s th sensor and DFC. If the fading vector \mathbf{h}_s is assumed to be TWDP distributed, then we can express,

$$\mathbf{h}_s^{\text{TWDP}} = \frac{\mathbf{u}(\phi_s)}{2\pi} \int_0^{2\pi} \check{\kappa}_s d\alpha + \frac{1}{2\pi} \check{\mathbf{h}}_s \int_0^{2\pi} \sqrt{1 - \check{\kappa}_s^2} d\alpha \quad (10)$$

where $\check{\kappa}_s = \sqrt{\frac{K_s[1+\Delta_s \cos \alpha]}{1+K_s[1+\Delta_s \cos \alpha]}}$ where Δ_s is the shape factor of the TWDP distributed propagation channel between the s th sensor and DFC, with the definitions of K_s and $\check{\mathbf{h}}_s$ remain unchanged. If \mathbf{h}_s is assumed to be double-Rayleigh distributed, K_s will be equal to 0 and therefore can be expressed as,

$$\mathbf{h}_s^{\text{DR}} = \prod_{j=1}^2 \check{\mathbf{h}}_{s_j}. \quad (11)$$

It is worth-mentioning that in this situation, no LOS component exist directly between indoor and outdoor antennas.

We also consider the sensors being uniformly deployed within a range of minimum distance of $d_{\min} = 400$ m and maximum distance of $d_{\max} = 1000$ m from the DFC. The large scale attenuation is characterized using $\beta_s = \nu_s \left(\frac{d_{\min}}{d_s}\right)^{\eta_P}$ where η_P is the pathloss exponent and ν_s is a log-normal variable such that $10 \log_{10}(\nu_s) \sim \mathcal{N}(\mu_P, \sigma_P^2)$ with $\mathcal{N}(\hat{\lambda}, \hat{\Sigma})$ representing normal distribution with mean vector $\hat{\lambda}$ and covariance matrix $\hat{\Sigma}$ respectively, d_s is the distance of the s th sensor from the DFC, μ_P and σ_P are the mean and standard deviations in dBm respectively. In the next subsection, we will use the values of $K_s, \Delta_s, \phi_s, \eta_P, \mu_P$ and σ_P recorded from the distributed MIMO measurement campaign to compare performance of different fusion rules proposed in [1].

The performance of WSN can be evaluated in terms of the conditional probability mass function (pmf) $P(\mathbf{x}|\mathcal{H}_i)$. Assuming conditionally independent and identically distributed (iid) decisions, we denote the probability of detection $P_{D,s} = P_{1,s}$ (or $P_D = P_1$) and false alarm $P_{F,s} = P_{0,s}$ (or $P_F = P_0$) at the s th sensor. We also assume that $P_{D,s} \geq P_{F,s}$ which refers to the fact that each sensor decision leads to receiver operating characteristics (ROC) above a particular decision threshold.

If Λ represents the fusion statistics and γ is the threshold with which the fusion statistics is compared to, then system probabilities of false alarm and correct detection can be defined as,

$$P_{F_0} \triangleq P(\Lambda > \gamma | \mathcal{H}_0) \quad \text{for False Alarm} \quad (12)$$

$$P_{D_0} \triangleq P(\Lambda > \gamma | \mathcal{H}_1) \quad \text{for Correct Detection.} \quad (13)$$

where $P(\cdot)$ and $p(\cdot)$ are used to denote probability and probability density functions (PDF); in particular $P(A|B)$ and $p(a|b)$ represent the probability of event A conditioned on event B and the pdf of random variable a conditioned on random variable b, respectively. We analyze fusion performance of the WSN in three different scenarios, a) both LOS and NLOS communication links exist between sensors and DFC (modeled by multipath Rician fading distribution), b) more than one dominant multipath component exist due to moving objects between sensors and DFC (fading characterized by TWDP distribution) and c) communication link between sensors and DFC suffering from keyhole effect (small scale channel variations modeled using double-Rayleigh distribution).

B. Fusion Rules

For comparison of fusion performance of a WSN, we consider two types of decision fusion rules. The first set of rules aims at concluding on the presence or absence of the target directly from the received signal without processing the transmit signal. For this kind of decision fusion, the optimum test statistics is given by [1],

$$\Lambda_{\text{opt}} = \ln \left[\frac{\sum_{\mathbf{x} \in X^S} \exp\left(-\frac{\|\mathbf{y} - \mathbf{H}\sqrt{\mathbf{B}}\mathbf{x}\|^2}{\sigma_w^2}\right) \prod_{s=1}^S P(x_s | \mathcal{H}_1)}{\sum_{\mathbf{x} \in X^S} \exp\left(-\frac{\|\mathbf{y} - \mathbf{H}\sqrt{\mathbf{B}}\mathbf{x}\|^2}{\sigma_w^2}\right) \prod_{s=1}^S P(x_s | \mathcal{H}_0)} \right] \quad (14)$$

assuming conditional independence of \mathbf{y} from \mathcal{H}_i and among the transmit signal vectors x_s . The second set of fusion rules firstly estimates the transmit signal from the received signal and then arrives at a global decision based on estimated transmit signal vector $\hat{\mathbf{x}}$ using Chair-Varshney (CV) rule. For noiseless channels, the CV test statistics is given by,

$$\Lambda_{\text{CV}} = \sum_{s=1}^S \left[\hat{\rho}_s \ln \left(\frac{P_{D,s}}{P_{F,s}} \right) + (1 - \hat{\rho}_s) \ln \left(\frac{1 - P_{D,s}}{1 - P_{F,s}} \right) \right] \quad (15)$$

where $\hat{\rho}_s \triangleq \frac{\hat{x}_s + 1}{2}$.

In the first group of fusion rules, we consider decision fusion under three different sub-optimum fusion rules, Maximal Ratio Combining (MRC), Equal Gain Combining (EGC) and Max-Log rules, the test statistics for each of which are given by,

$$\Lambda_{\text{MRC}} \propto \Re(\mathbf{1}_S^t (\mathbf{H}\sqrt{\mathbf{B}})^\dagger \mathbf{y}) \quad (16)$$

$$\Lambda_{\text{EGC}} = \Re((e^{j\angle(\mathbf{H}\sqrt{\mathbf{B}} \mathbf{1}_S)})^\dagger \mathbf{y}) \quad (17)$$

$$\Lambda_{\text{Max-Log}} = \min_{\mathbf{x} \in X^S} \left[\frac{\|\mathbf{y} - \mathbf{H}\sqrt{\mathbf{B}}\mathbf{x}\|^2}{\sigma_w^2} - \sum_{s=1}^S P(x_s | \mathcal{H}_0) \right] - \min_{\mathbf{x} \in X^S} \left[\frac{\|\mathbf{y} - \mathbf{H}\sqrt{\mathbf{B}}\mathbf{x}\|^2}{\sigma_w^2} - \sum_{s=1}^S P(x_s | \mathcal{H}_1) \right] \quad (18)$$

all assuming identical sensor performances. In the second group, we consider two different decoders to estimate $\hat{\mathbf{x}}$. With Maximum Likelihood (ML) detection, $\hat{\mathbf{x}}$ is obtained as,

$$\hat{\mathbf{x}}_{\text{ML}} = \arg \min_{\mathbf{x} \in X^S} \|\mathbf{y} - \mathbf{H}\sqrt{\mathbf{B}}\mathbf{x}\|^2 \quad (19)$$

while with Minimum Mean-Squared Error (MMSE) detection, $\hat{\mathbf{x}}$ is obtained as,

$$\hat{\mathbf{x}}_{\text{MMSE}} = \text{sign}[\bar{\mathbf{x}} + \mathbf{C}(\mathbf{H}\sqrt{\mathbf{B}})^\dagger ((\mathbf{H}\sqrt{\mathbf{B}})\mathbf{C}(\mathbf{H}\sqrt{\mathbf{B}})^\dagger + \sigma_w^2 \mathbf{I}_N)^{-1} (\mathbf{y} - \mathbf{H}\sqrt{\mathbf{B}}\bar{\mathbf{x}})] \quad (20)$$

where $\bar{\mathbf{x}} = E\{\mathbf{x}\}$ and $\mathbf{C} \triangleq \{(\mathbf{x} - \bar{\mathbf{x}})(\mathbf{x} - \bar{\mathbf{x}})^\dagger\}$ are the mean and covariance matrix of the transmit signal vector respectively. Once $\hat{\mathbf{x}}$ is obtained, we plug it in the CV-rule in (15) to obtain the test statistics for CV-ML and CV-MMSE rules .

C. Performance Comparison

In this subsection, the fusion performance of a WSN is investigated over realistic distributed MIMO mobile radio channels based on the collected measurements. Owing to majority in observation, for performance analysis of DF rules over \mathcal{SC} , \mathcal{DC} and \mathcal{SI} scenarios, we use Ricean, TWDP and double Rayleigh distributions to generate the channel fading vectors according to (9), (10) and (11) respectively.

1) *Receiver Operating Characteristics (ROC)*: The figures in this section represent the Receiver Operating Characteristics (ROC) (i.e., P_{D_0} v/s P_{F_0}) for the fusion rules presented in Section IV-B with $S = 8$ sensors and $N = 8$ antennas at the DFC under the channel SNR of 20 dB. We choose the channel SNR to be 20 dB, since from the measurement campaigns conducted in three different kinds of environments (\mathcal{SC} , \mathcal{SI} and \mathcal{DC}), the average attenuation calculated at any measurement location i , $\mathbf{A}(i)$ is found to be around 20 dB. The measured SNR over direct connection between the transmit and receive sounders is 40 dB. Therefore, the average resultant channel SNR should be around $(40 - 20) = 20$ dB.

- *Impact of large scale channel parameters*: For all the curves in Fig. 11 and Fig. 12, we consider the independent small scale fading vectors to be Rayleigh distributed i.e., $h_{n,s} \sim \mathcal{N}_{\mathbb{C}}(0, 1)$. We only change the large scale parameters to represent different scenarios. For the no shadowing condition ('Th'), we choose $(\eta_P, \mu_P, \sigma_P) = (1, 0 \text{ dB}, 0 \text{ dB})$. For other conditions we refer to Table I, i.e., for \mathcal{SC} , $(\eta_P, \mu_P, \sigma_P) = (2.72, 1.22 \text{ dB}, 2.4 \text{ dB})$, for \mathcal{SI} , $(\eta_P, \mu_P, \sigma_P) = (3.96, 1.48 \text{ dB}, 1.89 \text{ dB})$ and for \mathcal{DC} , $(\eta_P, \mu_P, \sigma_P) = (2.56, 1.77 \text{ dB}, 3.6 \text{ dB})$.

For the first group of rules, MRC and MaxLog (refer to Fig. 11), it is evident that for low shadowing and pathloss (Th and \mathcal{SC}) MaxLog looks an attractive solution. While, as we enter scenarios suffering from deep shadowing (\mathcal{SI} and \mathcal{DC}), MRC outperforms MaxLog. The reason can be attributed to the fact that the MaxLog rule is dependent on the noise spectral density σ_w^2 . Hence, the increase in pathloss and shadowing intensity results in poorer performance of MaxLog statistics owing to less signal strength. The MRC rule statistics are independent of σ_w^2 and depend only on the channel characteristics.

For the second group of rules, CV-ML and CV-MMSE (refer to Fig. 12), CV-MMSE always outperforms CV-ML while CV-ML performs equivalently under all propagation conditions. The reason for this odd behavior of CV-ML is due to the fact that the CV-ML statistics is only dependent on the channel SNR which is kept constant for all the curves. For CV-MMSE, the performance over \mathcal{SC} is better than that over \mathcal{DC} and \mathcal{SI} . The \mathcal{SC} experiences the lowest pathloss since the \mathcal{C} room is in the upper level with strong LOS communication paths. People moving in the room in the \mathcal{DC} scenario contributes to penetration losses resulting in higher pathloss than the \mathcal{SC} scenario.

- *Impact of small scale channel parameters* : For the curves in Fig. 13, Fig. 14 and Fig. 15, we consider independent small scale fading vectors to be Rayleigh distributed for the 'Th' case with large scale parameters of $(\eta_P, \mu_P, \sigma_P) = (1, 0 \text{ dB}, 0 \text{ dB})$. In Fig. 13, we compare the 'Th' set of results with fusion performance over 8×8 MIMO channel with Rician distributed fading vector and large scale parameters equivalent to \mathcal{SC} scenario i.e., $(\eta_P, \mu_P, \sigma_P) = (2.72, 1.22 \text{ dB}, 2.4 \text{ dB})$. The fading vectors are generated according to $\mathbf{h}_s^{\text{Rice}}$ with K_s randomly generated as $[K_{s,\min}, K_{s,\max}] = [0.5, 4]$. For Fig. 14, we generate the fading vector according to $\mathbf{h}_s^{\text{TWDP}}$ with K_s ran-

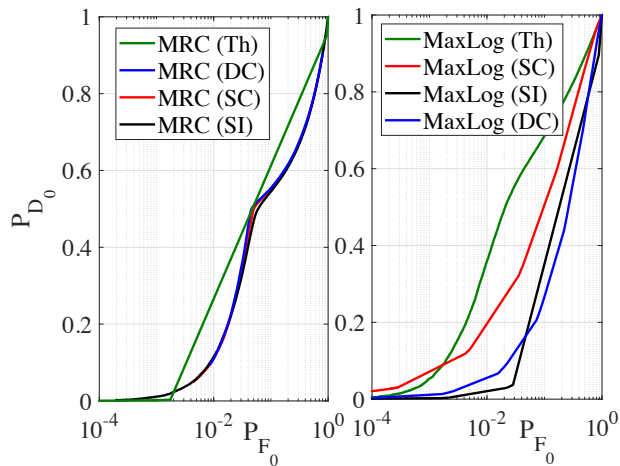


Fig. 11. Comparative ROC for the first group of fusion rules for different measured large scale parameters (varying η_P , μ_P and σ_P) with $S = 8$, $N = 8$ and Rayleigh distributed fading vector. Results for no shadowing condition, denoted by ‘Th’ are also plotted for comparison.

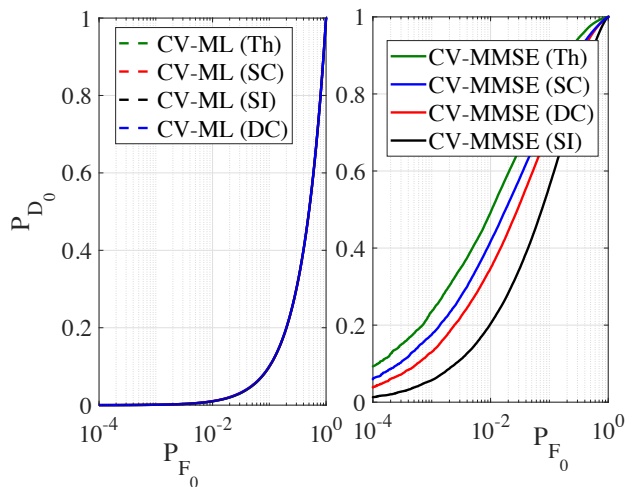


Fig. 12. Comparative ROC for the second group of fusion rules for different measured large scale parameters (varying η_P , μ_P and σ_P) with $S = 8$, $N = 8$ and Rayleigh distributed fading vector. Results for no shadowing condition, denoted by ‘Th’ are also plotted for comparison.

domly generated as $[K_{s,\min}, K_{s,\max}] = [6, 20]$ and Δ_s as $[\Delta_{s,\min}, \Delta_{s,\max}] = [0.1, 0.9]$ with large scale parameters equivalent to *DC* scenario i.e., $(\eta_P, \mu_P, \sigma_P) = (2.56, 1.77 \text{ dB}, 3.6 \text{ dB})$. For Fig. 15, the fading vectors are generated according to \mathbf{h}_s^{DR} i.e., double-Rayleigh distributed with large scale parameters equivalent to *SI* scenario i.e., $(\eta_P, \mu_P, \sigma_P) = (1.96, 1.48 \text{ dB}, 1.89 \text{ dB})$. These set of parameters are selected according to the values tabulated in Table III and Table I.

Under the ‘Th’ case, EGC performs better than MRC. In realistic scenarios, both fusion rules perform very close to each other. The CV-ML rule performs equivalently under all conditions due to the dependence of the CV-ML statistics on the channel SNR which is kept fixed for all curves. The MaxLog rule performs a bit better than CV-ML over Rician, TWDP and double-Rayleigh fading channels. MRC, EGC and CV-MMSE also perform very close to each other as long as there exists at least a group of strong LOS components between the transmitter and

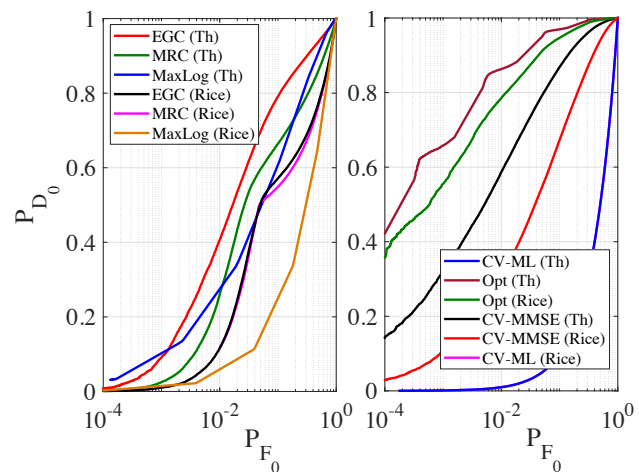


Fig. 13. Comparative ROC for all fusion rules for the *SC* environment with $S = 8$, $N = 8$ in Rician fading condition. Results for Rayleigh fading-only condition (‘Th’) are plotted for comparison.

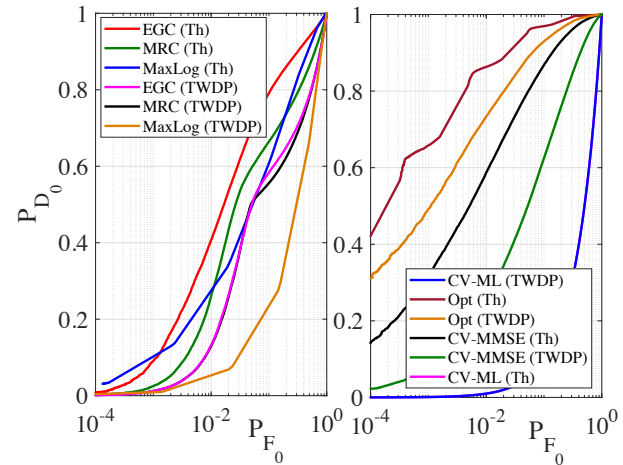


Fig. 14. Comparative ROC for all fusion rules for the *DC* environment with $S = 8$, $N = 8$ in TWDP fading condition. Results for Rayleigh fading-only condition (‘Th’) are plotted for comparison.

the receiver (Rician and TWDP fading cases). In case of DR, there exists no direct LOS component and in such a scenario, CV-MMSE really benefits over MRC/EGC from exploiting the local sensor performance information in the decoding stage.

Some analogies between performances under measured environment and simulated (as in [1]) can also be concluded from the results presented in Fig. 11 - Fig. 15. In both cases ROC performance demonstrates that CV-MMSE performs better than CV-ML rule, CV-MMSE performs close to MRC/EGC rules, while CV-ML exhibits the worst performance.

2) P_{D_0} v/s N : In Fig. 16 and Fig. 17, we show system probabilities of detection, P_{D_0} with two groups of fusion rules as an interpolated function of the number of receive antennas N under $P_{F_0} \leq 0.01$.

- *Impact of measurement environment*: For this set of figures, we consider large and small scale channel parameters from Table I and Table II for each kind of environment. We keep the channel SNR fixed at 20 dB. The saturation effect seen in [1] for all fusion rules under Rayleigh distributed fading-only condition is only

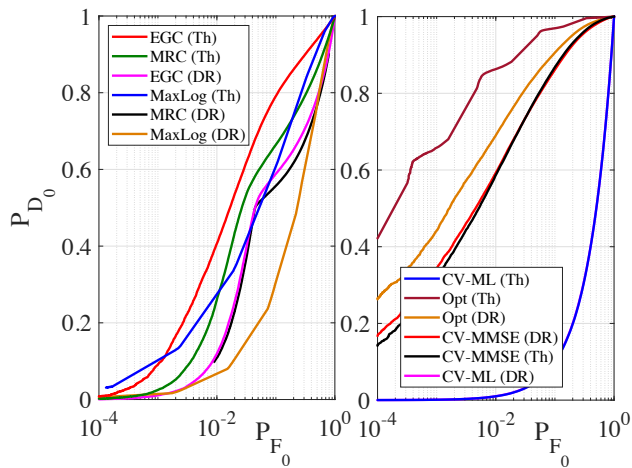


Fig. 15. Comparative ROC for all fusion rules for the SZ environment with $S = 8$, $N = 8$ in double-Rayleigh (DR) fading condition. Results for Rayleigh fading-only condition ('Th') are plotted for comparison.

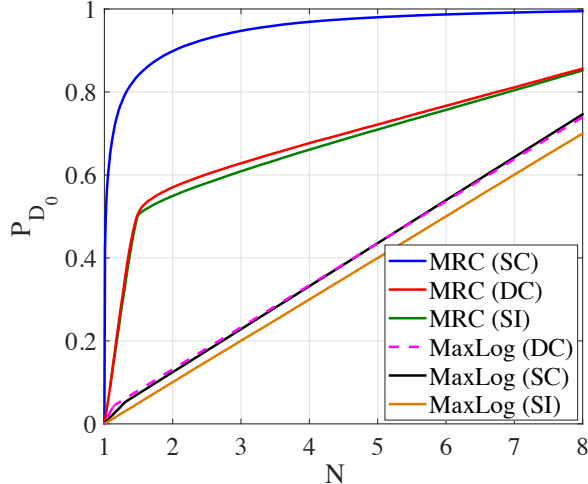


Fig. 16. P_{D_0} vs N for the first group of fusion rules with $S = 8$ for different measurement environments reflecting the impact of both large scale and small scale channel parameters.

exhibited by MRC and CV-MMSE rules for the SC condition. For the CV-ML and MaxLog rules, P_{D_0} increases proportionately with the increase in N for all scenarios. CV-MMSE and MRC rules exploit diversity gain both in SZ and DC scenarios and do not reach saturation for the values of N and the channel SNR considered. However, the increase in P_{D_0} is slower as N increases from 3 to 8 than as N increases from 1 to 3 (refer to Fig. 16 and Fig. 17).

V. CONCLUSION

The main goal of this paper is to investigate and study the practical implications of employing distributed MIMO based WSN, especially in the light of the recently proposed decision fusion algorithms for DFC equipped with multiple integrated antennas. This is accomplished through a measurement campaign comprising MIMO channel transmit-receive sounder, outdoor receive antennas mounted on a tower and unit antenna transmitters distributed in different kinds of indoor environments. The communication scenario is indoor-to-outdoor and fully-loaded (with equal number of transmit and receive

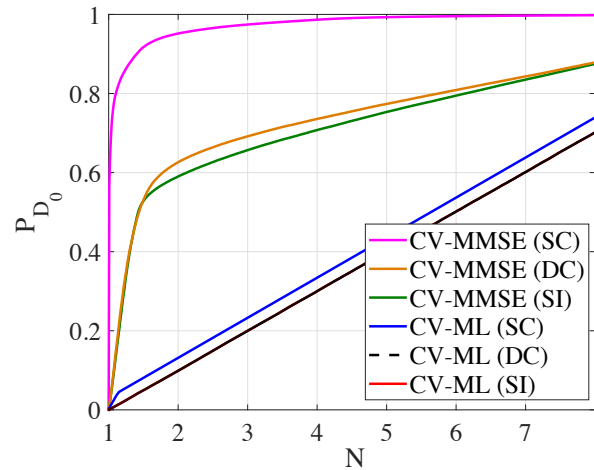


Fig. 17. P_{D_0} vs N for the second group of fusion rules with $S = 8$ for different measurement environments reflecting the impact of both large scale and small scale channel parameters.

antennas). The single antenna transmitters represent sensors while the receive set of antennas represent the DFC. The indoor environments can be static (no movement) or dynamic (movement of the people). Two different rooms are chosen that account for a wide variety of communication environments.

Both large and small scale channel statistics are captured for each measurement scenario and average values of pathloss and shadowing variations are calculated for all cases. For the small scale channel characteristics, 21.4% of the measurements fits the double Rayleigh, 28.6% follows the TWDP and remaining 50% fits the Rician distributions.

The large and small scale channel parameters encountered in the measured scenarios are directly incorporated in the performance analysis of two groups of fusion rules, Decode-and-fuse (MRC, EGC, MaxLog) and Decode-then-fuse (CV-ML and CV-MMSE) proposed in [1] for distributed MIMO MAC case. Over all scenarios, CV-ML performs worst while CV-MMSE is the most attractive choice. MRC and EGC perform very closely, while MaxLog performs worse than MRC/EGC. Nonetheless, all the fusion rules benefit from using multiple receive antennas and exploit diversity gain.

REFERENCES

- [1] D. Ciuonzo, G. Romano, and P. Salvo Rossi, "Channel-aware decision fusion in distributed MIMO wireless sensor networks: decode-and-fuse vs. decode-then-fuse," *IEEE Trans. Wireless Commun.*, vol. 11, no. 8, pp. 2976–2985, Aug. 2012.
- [2] D. Ciuonzo, P. Salvo Rossi, and S. Dey, "Massive MIMO channel-aware decision fusion," *IEEE Trans. Signal Process.*, vol. 63, no. 3, pp. 604–619, Feb. 2015.
- [3] B. Chen, L. Tong, and P. K. Varshney, "Channel-aware distributed detection in wireless sensor networks," *IEEE Signal Process. Mag.*, vol. 23, no. 4, pp. 16–26, Jul. 2006.
- [4] A. Lei and R. Schober, "Coherent Max-Log decision fusion in wireless sensor networks," *IEEE Trans. Commun.*, vol. 58, no. 5, pp. 1327–1332, May 2010.
- [5] D. Ciuonzo, A. Aubry, and V. Carotenuto, "Rician MIMO channel- and jamming-aware decision fusion," *IEEE Trans. Signal Process.*, vol. 65, no. 15, pp. 3866–3880, Aug. 2017.
- [6] B. Chen, R. Jiang, T. Kasetkasem, and P. K. Varshney, "Channel aware decision fusion in wireless sensor networks," *IEEE Trans. Signal Process.*, vol. 52, no. 12, pp. 3454–3458, Dec. 2004.

- [7] W. Li and H. Dai, "Distributed detection in wireless sensor networks using a multiple access channel," *IEEE Trans. Signal Process.*, vol. 55, no. 3, pp. 822–833, Mar. 2007.
- [8] P. Agrawal, A. Ahlén, T. Olofsson, and M. Gidlund, "Long term channel characterization for energy efficient transmission in industrial environments," *IEEE Trans. Commun.*, vol. 62, no. 8, pp. 3004–3014, Aug. 2014.
- [9] S. Wyne, A. P. Singh, F. Tufvesson, and A. F. Molisch, "A statistical model for indoor office wireless sensor channels," *IEEE Trans. Wireless Commun.*, vol. 8, no. 8, pp. 4154–4164, Aug. 2009.
- [10] T. Olofsson, A. Ahlén, and M. Gidlund, "Modeling of the fading statistics of wireless sensor network channels in industrial environments," *IEEE Trans. Signal Process.*, vol. 64, no. 12, pp. 3021–3034, Jun. 2016.
- [11] D. Rojas and J. Barrett, "Experimental analysis of a wireless sensor network in a multi-chamber metal environment," *Proc. European Wireless Conference 2016*, Oulu, Finland, May 2016, 6 pages.
- [12] H. Guo and Z. Sun, "Channel and energy modeling for self-contained wireless sensor networks in oil reservoirs," *IEEE Trans. Wireless Commun.*, vol. 13, no. 4, pp. 2258–2269, Apr. 2014.
- [13] P. K. Varshney, *Distributed Detection and Data Fusion*, 1st edition. Springer-Verlag, Inc., 1996.
- [14] M. Gastpar, M. Vetterli, and P. Dragotti, "Sensing reality and communicating bits: a dangerous liaison," *IEEE Signal Process. Mag.*, vol. 23, no. 4, pp. 70–83, July 2006.
- [15] J. F. Chamberland and V. V. Veeravalli, "Wireless sensors in distributed detection applications," *IEEE Signal Process. Mag.*, vol. 24, no. 3, pp. 16–25, May 2007.
- [16] R. Jiang and B. Chen, "Fusion of censored decisions in wireless sensor networks," *IEEE Trans. Wireless Commun.*, vol. 4, no. 6, pp. 2668–2673, Nov. 2005.
- [17] C. R. Berger, M. Guerriero, S. Zhou, and P. Willett, "PAC vs. MAC for decentralized detection using non-coherent modulation," *IEEE Trans. Signal Process.*, vol. 57, no. 9, pp. 3562–3575, Sep. 2009.
- [18] B. Chen, L. Tong, and P. K. Varshney, "Channel aware decision fusion in wireless sensor networks," *IEEE Trans. Signal Process.*, vol. 52, no. 12, pp. 3454–3458, Dec. 2004.
- [19] R. Jiang, S. Misra, B. Chen, and A. Swami, "Robust suboptimal decision fusion in wireless sensor networks," in *Proc. 2005 IEEE Military Communications Conference*, vol. 4, pp. 2107–2113.
- [20] M. K. Banavar, A. D. Smith, C. Tepedelenlioglu, and A. Spanias, "Distributed detection over fading MACs with multiple antennas at the fusion center," in *Proc. 2010 IEEE International Conference on Acoustics Speech and Signal Processing*, pp. 2894–2897.
- [21] X. Zhang, H. V. Poor, and M. Chiang, "Optimal power allocation for distributed detection over MIMO channels in wireless sensor networks," *IEEE Trans. Signal Process.*, vol. 56, no. 9, pp. 4124–4140, Sep. 2008.
- [22] R. Niu, B. Chen, and P. K. Varshney, "Fusion of decisions transmitted over Rayleigh fading channels in wireless sensor networks," *IEEE Trans. Signal Process.*, vol. 54, no. 3, pp. 1018–1027, Mar. 2006.
- [23] A. Lei and R. Schober, "Coherent max-log decision fusion in wireless sensor networks," *IEEE Trans. Commun.*, vol. 58, no. 5, pp. 1327–1332, May 2010.
- [24] C. Schneider, M. Narandzic, M. Kaeske, G. Sommerkorn, and R. S. Thomae, "Large scale parameter for the WINNER II channel model at 2.53 GHz in urban macro cell," in *Proc. IEEE Veh. Technol. Conf.*, May 2010, pp. 1–5.
- [25] J. Laurila, K. Kalliola, M. Toeltsch, K. Hugi, P. Vainikainen, and E. Bonek, "Wideband 3D characterization of mobile radio channels in urban environment," *IEEE Trans. Antennas Propag.*, vol. 50, no. 2, pp. 233–243, Feb. 2002.
- [26] F. Quitin, C. Oestges, F. Horlin, and P. De Doncker, "A polarized clustered channel model for indoor multi-antenna systems at 3.6 GHz," *IEEE Trans. Veh. Technol.*, vol. 59, no. 8, pp. 3685–3693, Oct. 2010.
- [27] F. Pei, J. Zhang, and C. Pan, "Elevation angle characteristics of urban wireless propagation environment at 3.5 GHz," in *Proc. IEEE Veh. Technol. Conf. (VTC Fall)*, Sep. 2013, pp. 1–5.
- [28] V. Kristem et al., "3D MIMO outdoor to indoor macro/micro-cellular channel measurements and modeling," in *Proc. IEEE Global Commun. Conf. (GLOBECOM)*, Dec. 2015, pp. 1–6.
- [29] D. S. Baum, H. El-Sallabi et al., "Final Report on Link Level and System Level Channel Models," *WINNER project deliverable D5.4 v1.0* Sep. 2005, v.1.4 Nov. 2005.
- [30] M. Dohler, "Virtual antenna arrays," Ph.D. dissertation, Kings College London, Nov. 2003.
- [31] V. Jungnickel et al., "Capacity measurements in a cooperative MIMO network," *IEEE Trans. Veh. Technol.*, vol. 58, no. 5, pp. 2392–2405, Jun. 2009.
- [32] A. R. Hammons, Jr., J. R. Hampton, N. M. Merheb, and M. Cruz, "Cooperative MIMO field measurements for military UHF band in low-rise urban environment," in *Proc. IEEE Workshop Sensor Array and Multichannel Signal Process.*, Darmstadt, Germany, Jul. 2008, pp. 122–126.
- [33] M. Webb, M. Yu, and M. Beach, "Propagation characteristics, metrics, and statistics for virtual MIMO performance in a measured outdoor cell," *IEEE Trans. Antennas Propag.*, vol. 59, no. 1, pp. 236–244, Jan. 2011.
- [34] S. Yoshida, K. Nishimori, T. Murakami, K. Ichihara and Y. Takatori, "Dynamic Group-based Antenna Selection for Uplink Multi-user MIMO in Distributed Antenna System," *IEICE Trans. Commun.* vol. E101-B, no. 7, pp. 1552-1560, 2018.
- [35] L. Ahumada, R. Feick, R. Valenzuela, and C. Morales, "Measurement and characterization of the temporal behavior of fixed wireless links," *IEEE Trans. Veh. Technol.*, vol. 54, no. 6, pp. 1913–1922, Nov. 2005.
- [36] W. C. Navidi, *Statistics for Engineers and Scientists*, 1st ed. New York, NY, USA: McGraw-Hill, 2006.
- [37] L. J. Greenstein, D. G. Michelson, and V. Erceg, "Moment-method estimation of the Ricean K-factor," *IEEE Commun. Lett.*, vol. 3, no. 6, pp. 175–176, Jun. 1999.
- [38] T. S. Rappaport, S. Y. Seidel, and K. Takamizawa, "Statistical channel impulse response models for factory and open plan building radio communicate system design," *IEEE Trans. Commun.*, vol. 39, no. 5, pp. 794–807, May 1991.
- [39] G. D. Durgin, T. S. Rappaport, and D. A. de Wolf, "New analytical models and probability density functions for fading in wireless communications," *IEEE Trans. Commun.*, vol. 50, no. 6, pp. 1005–1015, Jun. 2002.



I. Dey is currently a Marie Skodowska-Curie (EDGE) Fellow at Trinity College Dublin, Ireland. She performs her research in wireless communications at the Irish Research Centre for Future Networks and Communications (CONNECT). She received the M.Sc. degree in wireless communications from the University of Southampton, Southampton, U.K., in 2010, and the Ph.D. degree in electrical engineering from the University of Calgary, Calgary, Canada, in 2015. From 2015 to 2016, she was a Post-Doctoral Research Fellow with the Ultra-Maritime

Digital Communication Center, Dalhousie University, Canada. She was a Research Fellow with the Department of Electronics and Telecommunications, Norwegian University of Science and Technology, Trondheim, Norway, from 2016 to 2017. Her current research interests include channel modeling, channel estimation and prediction, adaptive modulation, and dirty tape coding for different wireless propagation environments, and wireless sensor networks. In 2016, she received the prestigious Alain Bensoussan research fellowship from the European Research Consortium for Information and Mathematics (ERCIM).



P. Salvo Rossi was born in Naples, Italy, on 26 April 1977. He received the Dr.Eng. degree in telecommunications engineering (summa cum laude) and the Ph.D. degree in computer engineering, in 2002 and 2005, respectively, both from the University of Naples Federico II, Italy. From 2005 to 2008, he worked as a postdoc at the Department of Computer Science and Systems, University of Naples Federico II, Italy, at the Department of Information Engineering, Second University of Naples, Italy, and at the Department of Electronics and Telecommunications,

Norwegian University of Science and Technology, Norway. From 2008 to 2014, he was an assistant professor (tenured in 2011) in telecommunications at the Department of Industrial and Information Engineering, Second University of Naples, Italy. From 2014 to 2016, he was an associate professor in signal processing with the Department of Electronics and Telecommunications, Norwegian University of Science and Technology, Norway. From 2016 to 2017, he was a full professor in signal processing with the Department of Electronic Systems, Norwegian University of Science and Technology, Norway. Since 2017, he is a principal engineer with the Department of Advanced Analytics and Machine Learning, Kongsberg Digital AS, Norway. He held visiting appointments at the Department of Electrical and Computer Engineering, Drexel University, US, at the Department of Electrical and Information Technology, Lund University, Sweden, at the Department of Electronics and Telecommunications, Norwegian University of Science and Technology, Norway, and at the Excellence Center for Wireless Sensor Networks, Uppsala University, Sweden. He is an IEEE senior member and serves as a senior editor for the IEEE Communication Letter (since 2016) and an associate editor for the IEEE Transactions and Wireless Communication (since 2015). He was an associate editor for the IEEE Communication Letter (from 2012 to 2016) and a Guest Editor for Elsevier Physical Communication (2012). His research interests fall within the areas of communications, machine learning and signal processing.



M. Majid Butt (S'07 – M'10 – SM'15) received the MSc degree in Digital Communications from Christian Albrechts University, Kiel, Germany, in 2005, and the PhD degree in Telecommunications from the Norwegian University of Science and Technology, Trondheim, Norway, in 2011. He is senior scientist 5G+ research at Nokia Bell Labs, France, as well as, a visiting research Assistant Professor at Trinity College Dublin, Ireland. Before that, he has held various positions at University of Glasgow, UK, Trinity College Dublin, Ireland, Fraunhofer

HHI, Germany and University of Luxembourg. He is recipient of Marie Curie Alain Bensoussan postdoctoral fellowship from European Research Consortium for Informatics and Mathematics (ERCIM). Dr. Majid's major areas of research interest include communication techniques for wireless networks with focus on radio resource allocation, scheduling algorithms, energy efficiency and machine learning for RAN. He has authored more than 60 peer reviewed conference and journal publications in these areas. He has served as organizer/chair for various technical workshops on various aspects of communication systems in conjunction with major IEEE conferences including WCNC, Globecom and Greencom. He is a senior member of IEEE and serves as an associate editor for IEEE Access journal and IEEE Communication Magazine since 2016.



N. Marchetti is currently Assistant Professor in Wireless Communications at Trinity College Dublin, Ireland. He performs his research under the Irish Research Centre for Future Networks and Communications (CONNECT), where he leads the Wireless Engineering and Complexity Science (WhyCOM) lab. He received the PhD in Wireless Communications from Aalborg University, Denmark in 2007, and the M.Sc. in Electronic Engineering from University of Ferrara, Italy in 2003. He also holds an M.Sc. in Mathematics which he received from Aalborg

University in 2010. His collaborations include research projects in cooperation with Nokia Bell Labs and US Air Force Office of Scientific Research, among others. His research interests include Adaptive and Self-Organizing Networks, Complex Systems Science for Communication Networks, PHY Layer, Radio Resource Management. He has authored 120 journals and conference papers, 2 books and 7 book chapters, holds 2 patents, and received 4 best paper awards. He is a senior member of IEEE and serves as an associate editor for the IEEE Internet of Things Journal since 2018 and the EURASIP Journal on Wireless Communications and Networking since 2017.